3D Digital Outcrop Model reconstruction of the Kimberley outcrop (Gale crater, Mars) and its integration into Virtual Reality for simulated geological analysis

Gwénaël Caravaca, Stéphane Le Mouélic, Nicolas Mangold, Jonas L'Haridon, Laetitia Le Deit, Marion Massé

3D DIGITAL OUTCROP MODEL RECONSTRUCTION OF THE KIMBERLEY OUTCROP (GALE CRATER, MARS) AND ITS INTEGRATION INTO VIRTUAL REALITY FOR SIMULATED GEOLOGICAL ANALYSIS

Gwénaël Caravaca[1, *], Stéphane Le Mouélic[1], Nicolas Mangold[1], Jonas L'Haridon[1,†], Laetitia Le Deit[1], Marion Massé[1]

[1] *Laboratoire de Planétologie et Géodynamique, UMR 6112 CNRS, Université de Nantes, Université Angers, 2 Rue de la Houssinière, 44322 Nantes Cedex 3, France*

[†] *Current address: European Science Foundation, 1 Quai Lezay-Marnesia, 67000 Strasbourg, France*

*Corresponding author. Contact details for corresponding author: Phone: +33.2.51.15.54.32 E-mail: gwenael.caravaca@univ-nantes.fr

Abstract

Structure-from-Motion photogrammetry has recently become a cheap and efficient method to reconstruct accurate and highly-resolved 3D Digital Outcrop Model (DOM) from a single set of images. This enables the 3D visualization of hardly accessible and/or remote geological scenes, which is of strong interest for planetary bodies. This paper focuses on the reconstruction of the DOM of the Kimberley outcrop (Gale crater, Mars) using the Agisoft PhotoScan Professional software. This software is used to compute an accurate, scaled and georeferenced 3D mesh of this outcrop from set of multi-scale images taken by the Mars Science Laboratory rover *Curiosity*. This model was merged with a 3D model computed from orbital images from the High Resolution Imaging Science Experiment camera (HiRISE) to

provide the context. One of the challenges is to integrate data coming from different cameras (with varying optical parameters) not specifically designed for 3D rendering, and with limited points of views. While the obtained DOM allows to observe and characterize geological features of Kimberley's sedimentary series, classic viewing methods through a 2D screen limits the understanding of the real 3D geometry and scale of the outcrop, as there is no feature such as trees or roads on Mars to provide size references to the user. To overcome this issue and facilitate the interpretation of the DOM, the latter is integrated into a Virtual Reality (VR) environment that enables one or several users working in a collaborative mode to experience a real scale, reliable and realistic depiction of the actual geometries of the geological features reconstructed on the mesh. Precise and accurate description, contextualization of the samplings and mapping of the Kimberley outcrop can therefore be achieved in VR allowing for more precise characterization and interpretations, the same way one would do on a real geological field trip.

Keywords: Mars, Gale crater, Curiosity, Digital Outcrop Model, Virtual Reality, geological mapping.

1. Introduction

In the recent years, Structure-from-Motion (SfM) photogrammetry became popular as a fast, cheap and efficient way to reconstruct 3D photorealistic meshes of geological features and/or Digital Outcrop Models (DOM; e.g. Arbués *et al.*, 2012; Favalli *et al.*, 2012; Westoby *et al.*, 2012, Carrivick, *et al.*, 2016). This technique relies on the projection of tie-points recognized across a set of overlapping images taken from different points of view, thus recreating their position within a 3D space. Therefore, any structure can be reconstructed using a set of purposely taken and optimized images (e.g. Verhoeven, 2011; Arbués *et al.*, 2012;

51 Triantafyllou *et al.*, 2019), or even a set of non-optimized images providing a minimum
52 overlapping (e.g. Tavani *et al.*, 2014).

53 This method is more and more used in geosciences thanks to the availability of different
54 software solutions (Martell *et al.*, 2018), and the increasing processing power of computers and
55 their graphic cards. Using SfM photogrammetry, we obtain photorealistic 3D meshes allowing
56 to virtually reconstruct geological features of varying sizes, from mm-scale samples to km-scale
57 outcrops (Verhoeven, 2011; Favalli *et al.*, 2012; Westoby *et al.*, 2012; Carrivick *et al.*, 2016).
58 The major interest lies on the ability to reconstruct structures that would be hardly accessible
59 for analysis otherwise e.g. caves as in Triantafyllou *et al.*, 2019, mines as in Vrublová *et al*.,
60 2015, volcanic edifices as in Carr *et al*., 2019, but also remote and/or dangerous environments
61 and other planets. In the latter cases image acquisition may heavily relies on the use of UAVs
62 or autonomous rovers.

63 SfM photogrammetry appears particularly suited for the remote exploration and
64 characterization of planetary bodies such as Mars. Indeed, several previous works have shown
65 that photographic material produced by the robotic landers and rovers on Mars can be used to
66 digitally rebuild the surface (e.g. Ostwald & Hurtado, 2017) and characterize several important
67 features leading to paleoenvironmental interpretation, for instance aeolian bedforms of the
68 Martian Stimson Fm. in Gale crater (Banham *et al.*, 2018). Using a digitally reconstructed 3D
69 DOM is a helpful tool for the study of remote planetary outcrops. Indeed, this technique allows
70 to depict an accurate view of the overall geometries and shape of the targeted outcrop under
71 many different angles and points of view. However, the use of conventional 2D flat screens and
72 their inherent projection biases tends to reduce the interest of such a tool. Hence, the availability
73 of Virtual Reality (VR) headsets now provides the possibility to go one step further. Indeed, the
74 integration within a VR environment allows to properly visualize at real scale and without
75 deformation the reconstructed DOM and to provide a more realistic sense of the geometries of

the outcrop. Yet only few VR applications fully dedicated to Geosciences exist so far (e.g. Gerloni *et al.*, 2018; Billant *et al.*, 2019), highlighting the need for such tools to be developed as an effort to open the way to the geological exploration and characterization of remote outcrops using their digital recreation.

In this work, we focus on the reconstruction of the Kimberley outcrop analyzed by the Mars Science Laboratory (MSL) rover *Curiosity* in the Gale crater (Fig. 1). This outcrop presents a siliciclastic series whose stratigraphic relations with its immediate surroundings are still poorly constrained, yet critical for the paleoenvironmental interpretation of the area and of the processes behind its formation (e.g. Grotzinger et al., 2015, Fraeman *et al.*, 2016; Le Deit *et al.*, 2016). Using a large dataset of images produced by the *Curiosity* rover, we aim at reconstructing the most accurate multi-scale DOM possible of the Kimberley outcrop. Then, we integrated it within a collaborative VR environment to assess the potential of a simulated "*in situ*" geological characterization millions of km away and improve the related geological interpretations.

2. Localization and geological setting of the Kimberley outcrop

Gale crater is a 154 km-wide impact crater situated close to the crustal dichotomy boundary of Mars which separates heavily cratered uplands to the South and sparsely cratered lowlands to the North. The MSL rover *Curiosity* landed in the northern part of Gale crater on Mars in 2012 (Fig. 1a) and explored the geology of Aeolis Palus and the lowermost part of Aeolis Mons (informally named Mount Sharp) along a 20 km-long traverse (Fig. 1b). The analysis of sedimentary rocks concludes for the presence of fluvio-deltaic and lacustrine depositional environments along a >300 m thick sedimentary unit presumably formed ~3.4-3.7 billion years ago (e.g. Grotzinger *et al.*, 2014, 2015; Le Deit *et al.*, 2016; Stack *et al.*, 2016; Rice *et al.*, 2017; Stein *et al.*, 2018; Bristow *et al.*, 2018).

However, the sedimentary succession recorded in Gale crater remains for a part uncertain, with somewhat crucial implication for the overall history of this past basin. This is notably the case of the Kimberley outcrop, studied by *Curiosity* in 2014 between sols 597 and 630, a "sol" being a Martian day (Fig. 1b and 1c; Rice *et al.*, 2017). The outcrop shows siliciclastic series recording fluvial settings as many outcrops observed since Bradbury Landing (Fig. 1b; Le Deit *et al.* 2016; Stack *et al.*, 2016, Rice *et al.*, 2017). Yet, this specific outcrop stands out by the unusually high abundance of potassium (2-5 wt.% of K_2O) analyzed in these clastic sediments (Le Deit *et al.*, 2016), contrasting with other sedimentary rocks with mafic composition lacking the high abundance in potassium (e.g. Mangold *et al*., 2017).

While the origin of the high potassium abundance might likely be detrital (Treiman *et al.*, 2016), the question of the local to regional stratigraphical relationship of this outcrop with the rest of the Gale sedimentary series remains open to further investigation in absence of continuity in outcrops and clear contact with other units. Using orbital data, Williams *et al.* (2018) proposed that the uppermost sections of the Kimberley outcrop were actually part of a younger geological unit postdating the lacustrine deposits encountered later on the rover path and their subsequent erosion, suggesting a major unconformity within the Kimberley sequence. In order to better constrain the structure, geometry and facies of this outcrop, we focused our work on the photorealistic reconstruction of a multiscale DOM of the Kimberley outcrop area, and its integration in VR using all the available ground-based imagery (*Curiosity*) and Digital Elevation Model (DEM) from orbital imagery for the broader regional context.

Figure 1 (color online, 1 column):

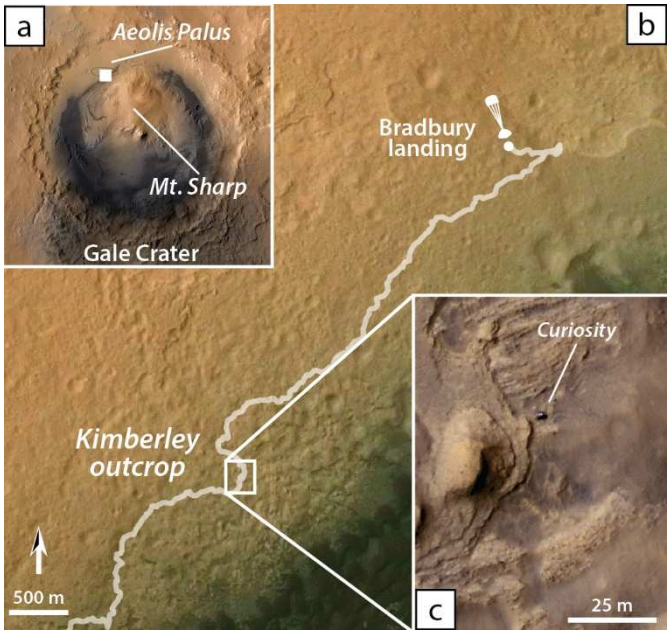

Figure 1: Localization of the studied area on Mars. a) White square represents the area of operations of Mars Science Laboratory rover *Curiosity* in the Gale crater. b) White line shows the first part of rover's traverse since its Bradbury landing in August 2012 and the location of the Kimberley outcrop visited in 2014 between sols 597 and 630 (base image: NASA / JPL / MSSS / ESA / DLR / FU Berlin (G. Neukum) / Tanya Harrison / Emily Lakdawalla). c) C*uriosity* rover at Kimberley during sol 595 as seen from orbit by Mars Reconnaissance Orbiter's HiRISE camera (base image: HiRISE ESP_036128_1755 full color tile, NASA/JPL/University of Arizona, https://www.uahirise.org/ESP_036128_1755).

3. Materials & Methods

3.1. Imaging dataset

The MSL rover *Curiosity* is equipped with 17 cameras (e.g. Alexander & Deen, 2015). The most useful for our purpose are the pair of navigation cameras (Navcam), the mast cameras (Mastcam), and the Mars Hans Lens Imager (MAHLI). The Navcam and Mastcam are mounted atop of the 2 meters high remote sensing mast (Fig. 2a). The MAHLI is situated on the mobile

140 robotic arm of the rover. These cameras have been designed for different objectives. Their
141 respective optical parameters (e.g. resolution, focal field, etc.) are summarized in Table 1.
142 Figure 2b compares the respective field of views of the remote sensing mast cameras. These
143 differences in optical parameters complicates the photogrammetric processing. Indeed, a
144 continuous set of similar parameters, most notably the focal length, is preferred to improve the
145 overall efficiency of the photogrammetric process for it computing the point's spatial
146 projection using the focal length information (Ullman, 1979).

147 The Navcam greyscale wide angle stereo pair analyzes the vicinity of the rover to
148 determine the trafficability of the area (Maki *et al.*, 2012) and to identify the scientific targets.
149 Both full frame images (1024x1024 pixels wide, "NAV") and degraded versions (256x256
150 pixels wide, "TRAV") taken by the Navcam are considered, "TRAV" version being acquired
151 during each displacement of the rover. The latter are very useful as they contain a significant
152 overlap and often serve to connect the whole set of images. Straightforward results for
153 photogrammetric reconstruction are generally obtained with Navcam images, as they are
154 systematically acquired as a stereoscopic pair using left and right cameras. Navcam greyscale
155 images are useful to reconstruct terrains, but generally show only a low level of fine-scale
156 details (Table 1, Fig. 2b), restraining their use for science purposes.

157 The full color high-resolution Mastcam34 wide angle and Mastcam100 telelenses are a
158 pair of cameras designed to retrieve more precise scientific information from the surroundings.
159 But unlike the Navcam pair, their different focal lengths (34 mm and 100 mm; Table 1) result
160 in poorly overlapping images (Fig. 2b). These differential images thus restrict straightforward
161 photogrammetric reconstruction despite their obvious interest given their resolution.

162 The MAHLI is a color high-resolution microscope. It can be operated locally to take
163 images with a good overlap and different viewing angles, allowing an accurate reconstruction

of very small-scale geological features (e.g. Edgett *et al.*, 2015; Ostwald & Hurtado, 2017; Table 1).

Table1:

Instrument	Common designation	Colorization	Resolution	Focal length	Field of view	Reference
Navigation Cameras	NavCam	Greyscale	1024 x 1024 px (256 x 256 px for "TRAV")	14.67 mm	45° x 45°	Maki *et al.*, 2012
Mast Camera (left)	MastCam left (ML or M-34)	RGB	1600 x 1200 px	34 mm	18.4° x 15°	Malin *et al.*, 2010; Bell *et al.*, 2013
Mast Camera (right)	MastCam right (MR or M-100)	RGB	1600 x 1200 px	99.9 mm	6.3° x 5.1°	Malin *et al.*, 2010; Bell *et al.*, 2013
MArs Hand Lens Imager	MAHLI	RGB	1600 x 1200 px	18.4 mm	26.8° x 20.1° to 31.1° x 23.3°	Edgett *et al.*, 2015

Table 1: Optical parameters of the Navcam, Mastcam and MAHLI imagers on board *Curiosity* used to take the images used to photogrammetrically reconstruct the Kimberley DOM.

Figure 2 (color online, 1.5 column):

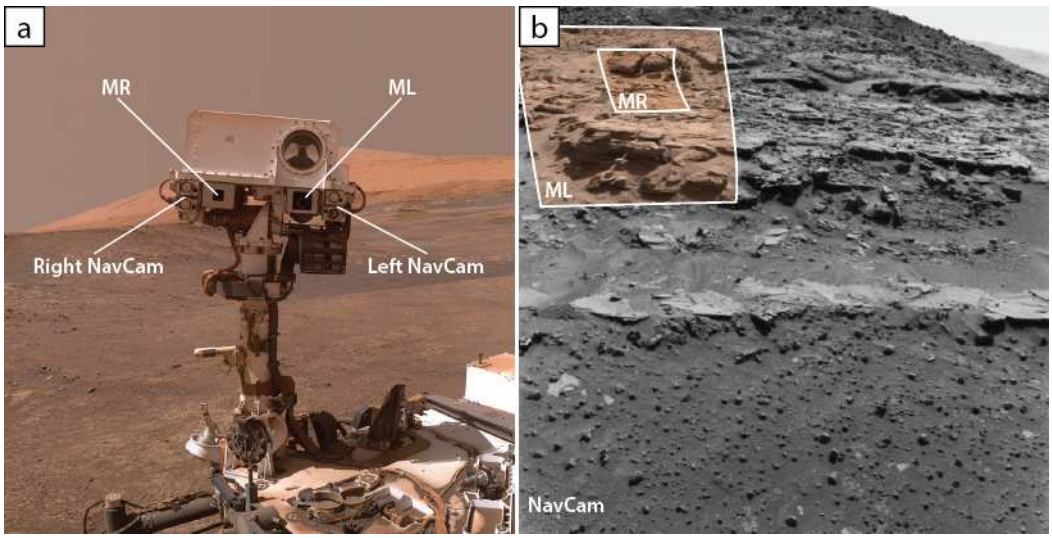

Figure 2: a) Detail of the "selfie" picture of *Curiosity* taken on sol 1943 by the MAHLI imager, showing the mast of the rover, supporting the position of the different Navcam and Mastcam imagers. ML: left Mastcam, focal length = 34 mm; MR: right Mastcam, focal length = 100 mm. (base image PIA22207, NASA/JPL-Caltech/MSSS,

https://photojournal.jpl.nasa.gov/catalog/pia22207). b) Composite image showing the variations in resolution, colorization and field of view of the different Navcam and Mastcam (MR and ML) imagers on board *Curiosity* for a given target between sols 603 and 604 (images 0604MR0025500120400908E01_DRCL, 0603ML0025450060301382E01_DRCL and NLB_451026778RADLF0311094NCAM00271M1)

The imagery dataset used in this work consists in 2005 images of the MSL archive taken during sols 597 to 630. We use 638 Navcam images, 1505 Mastcam images (890 Mastcam left, 615 Mastcam right) and 32 MAHLI images. All those images are publicly available on the Planetary Data System (PDS) servers (https://pdsimg-3.jpl.nasa.gov/w10n/msl/).

Orbital images used in this study are from the High Resolution Imaging Science Experiment images (HiRISE; McEwen et al., 2007) onboard the Mars Reconnaissance Orbiter. We use an extract of the public HiRISE DEM with a resolution of 1 m/pixel (Parker & Calef III, 2016), draped by a colorized version of the HiRISE visible orthoimage with a resolution of 25 cm/pixel (Calef III & Parker, 2016).

3.2. Softwares and Structure-from-Motion processing

Preprocessing of the raw dataset (see further) is performed using both the IMG2PNG command-line software (available at: http://bjj.mmedia.is/utils/img2png/) and the ExifTool software (Harvey, 2013). The SfM photogrammetry relies on a suite of algorithms designed to transform a set of multiple overlapping images into geometric 3D meshes (Ullman, 1979; see online supplementary material appendix A2 and Fig. S1) and is particularly powerful and suited to reconstruct geological outcrops (e.g. Westoby *et al.*, 2012; Bemis *et al.*, 2014; Micheletti *et al.*, 2015). In this work, we use Agisoft PhotoScan Professional (v. 1.4.4, Agisoft LLC, 2018), one of the most widely used SfM solution in the community for geological applications (e.g.

Verhoeven, 2011; Arbués *et al.*, 2012; Tavani *et al.*, 2014; Ostwald & Hurtado, 2017; Triantafyllou *et al.*, 2019). We use the CloudCompare software (v.2.9, Girardeau-Montaut, 2015) for comparison and validation of the scale, orientation and elevation of the obtained DOM against pre-existing calibrated model such as the orbital-derived DEM.

4. Reconstruction of the Kimberley DOM

4.1 Preprocessing of the imagery dataset

Raw images downloaded from the PDS have already been subject to a minimal but necessary linearization and radiometric correction before their release (Alexander & Deen, 2015). Hence, no further specific treatment nor colorimetric correction is needed and therefore is not performed here. However, the raw data downloaded from the PDS archive need to be converted into files readable by PhotoScan. The .IMG raw image data are converted into.TIFF files using IMG2PNG. Then, EXIF metadata extracted from the .LBL label files such as focal length, pixel size and geographic coordinates (projected into the IAU Mars 2000 spherical projection; Seidelmann *et al.*, 2002) are incorporated into the .TIFF images using ExifTool. Lastly, an alpha-layer mask is added to .TIFF images to mask rover elements present in the field of view, either automatically for Navcam images as masks are procedurally generated and already available on the PDS (Alexander & Deen, 2015), or manually drawn in the case of Mastcam images. The metadata information and alpha-layer masks are then considered by the PhotoScan during the alignment process to enhance treatment efficiency.

4.2. Cameras alignment and sparse point cloud generation

The variations in optical parameters between the different MSL cameras prevent any automated optimal alignments of the whole set of images during the first step of the photogrammetric process. In addition, several other important limits are inherent to the images taken by the rover: non-optimal or inadequate points of view, non-overlapping images, non-consecutive views and/or changing lighting. To handle this problem, we first took advantage of the software's embedded advanced geospatial features to preposition the images into its workspace (Fig. 3a), using images geographic coordinates retrieved from the PDS data. More processing power is thus allowed to the recognition of tie-points as the exact location of the camera is already known and set. Moreover, as the geographic coordinates for each photo are known, PhotoScan is able to produce a geographically constrained and scaled model. Figure 4a shows the positions of the georeferenced Navcam images within PhotoScan's workspace (Fig. 3a right), perfectly mirroring the traverse of *Curiosity* as obtained from the PDS data (Fig. 3a left).

240 Figure 3 (color online, 2 columns):

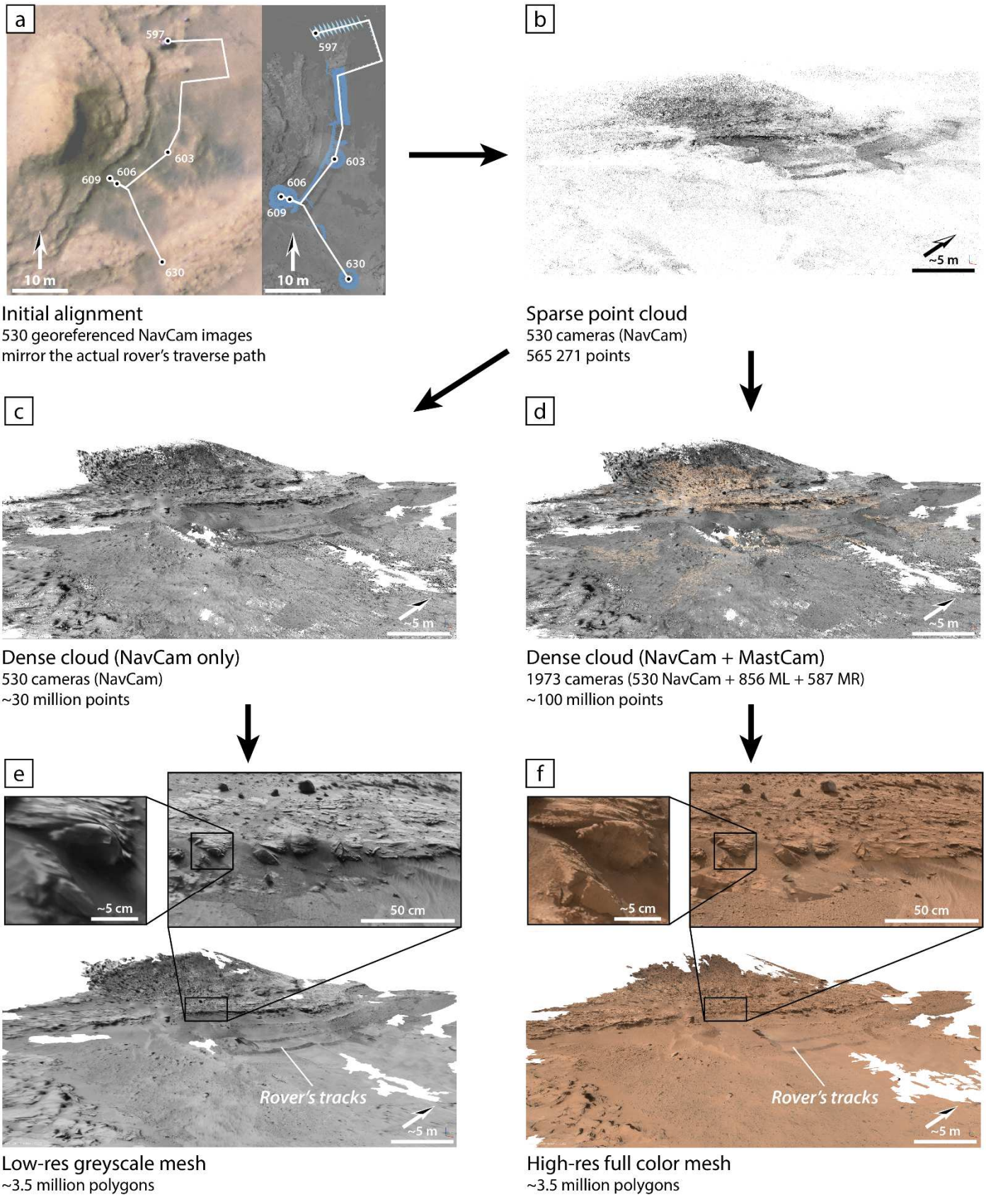

Figure 3: a) Georeferencing of the entry images within PhotoScan allows to constrain the position of the cameras within the software's workspace. Left: actual path of *Curiosity*'s traverse between sols 597 and 630 (white line; base image: HiRISE ESP_036128_1755_COLOR full color tile, NASA/JPL/University of Arizona, https://www.uahirise.org/ESP_036128_1755). Right: position of 530 aligned Navcam images (blue frames) within PhotoScan's workspace, mirroring the rover's real traverse. b) Sparse point cloud obtained after alignment of 530 Navcam greyscale images. c) Dense cloud obtained from the aligned Navcam greyscale images. d) Dense cloud obtained using 530 Navcam greyscale images and 1443 Mastcam color images, based on the position of the Navcam images from the initial alignment. e) Low-resolution greyscale mesh triangulated from the Navcam dense cloud. Detail shows that resolution is limited to the dm-scale, providing a blurry and inaccurate mesh under that level. f) High-resolution full color mesh triangulated from the Navcam plus Mastcam dense cloud. Detail shows a higher resolution (up to the sub-cm-scale), providing a sharp and accurate model even in very close range.

A first alignment is computed using only the 638 Navcam images. After several iterations of the alignment process, first with the "TRAV" degraded Navcam products only, and then with all the Navcam images ("TRAV" and "NAV"), we obtain a first sparse point cloud (Fig. 3b) composed by ~565 k points with 530 cameras aligned out of 638 (~83 %). The general shape and form of the Kimberley outcrop is recognizable on this sparse cloud, with a highest density of points located in the central part of the outcrop, where a more important number of images of greater quality were acquired (Fig. 3b). At this stage, outliers can be identified as well as misaligned cameras by direct comparison with the source 2D images and are therefore removed. The position of the aligned Navcam cameras is saved for further steps.

4.3. Dense clouds generation

From these alignments and sparse point cloud, a dense point cloud is computed (Fig. 3c). This cloud is composed of ~30.3 M points representing a precise spatial coverage of the Kimberley outcrop area. The level of detail varies as per the density of images for a targeted object and the distance where the images were taken from. Furthermore, this dense cloud is only in greyscale according to the Navcam images colorization. Its resolution is not sufficient enough to fulfill our scientific needs. In order to reconstruct the most accurate and precise DOM possible for the Kimberley outcrop, we need to also integrate Mastcam wide angle and telelens color images.

Mastcam images cannot be correctly aligned if treated simultaneously with the set of Navcam images, due to the lack of overlap and the significant difference in focal length (14.67 mm *vs* 34 mm *vs* 100 mm; Table 1 and Fig. 2b) or illuminating conditions. Still, the Mastcam imagers are situated very close to the Navcam imager on *Curiosity*'s mast, resulting in a very close position of the cameras and a relatively similar viewpoint when imaging the same targets (see Fig. 2a). Therefore, in order to get an alignment on the Mastcam images, we first reimported in our workspace the previously saved position of the 530 aligned Navcam cameras. PhotoScan was then able to realign and project ~96 % of the Mastcam images (856/890 and 587/615 for the ML and MR, respectively), resulting in a highly detailed dense point cloud (Fig. 3d). This dense cloud differs from the previously obtained cloud using only Navcam by the number of points available (~100 M points) and by a much higher level of detail, while the spatial extent covered by the model remains similar (~2780 m²).

4.4. Mesh generation, texturing and export

The next step in the photogrammetric reconstruction process is to generate a 3D mesh from each of the dense point clouds. As to compare the variation in resolution and quality of

291 the resulting mesh, similar parameters are set: a count of ~3.5 million of polygons and a texture
292 composed of 8 tiles with a size of 8192x8192 pixels each.

293 The mesh in Figure 4e has been triangulated from the Navcam only dense cloud (Fig.
294 3c) and textured accordingly using Navcam imagery only. Similarly to the dense cloud, the
295 DOM shows a good spatial coverage: geological structures of the outcrop (e.g. sandstone beds)
296 are identifiable, as well as the tracks made by *Curiosity* on Martian dust. However, several
297 holes in the model are present, due to gaps in the projection of the original images that the
298 software could not interpolate correctly (Fig. 3e). They were already present in the dense cloud
299 (Fig 3c). The resolution of the model and its associated textures allows us to observe a level of
300 details down to the 10 cm-scale (Fig. 4e). Under that limit, textures become too blurry to
301 distinguish any significant feature (e.g. pebbles). The mesh itself is not resolved enough to
302 accurately reproduce the shape of the objects (e.g. the sandstone bed detailed in Fig. 4e that is
303 identifiable at midrange but becomes indistinguishable in a close-up view).

304 The mesh in Figure 4f has been triangulated from the Navcam plus Mastcam dense
305 cloud (Fig. 3d) and textured using Mastcam color imagery only. The full color texturing of this
306 DOM is a significant improvement over the other mesh (Fig. 3e) as it allows both to observe
307 real colors and to see much finer details of this Martian outcrop. Like its lower resolution
308 counterpart (Fig. 3e), this DOM provides a good spatial coverage of the outcrop area. However,
309 fewer holes can be observed, enhancing the overall quality of the mesh (Fig. 3f). This DOM
310 shows a much higher resolution in the mesh and textures allowing the visualization of details
311 at cm-scale, revealing key-features for the scientific investigation. For example, the same
312 sandstone bed that appeared blurry and roundish in the Navcam DOM (detail on Fig. 3e) now
313 shows sharp edges on this highly resolved mesh (detail on Fig. 3f). This DOM allows us to
314 observe geological features at the cm-scale all over the reconstructed area, and below the-cm-
315 scale on specific points where the rover obtained short-range images. Nevertheless, its

316 resolution varies and decreases toward the edge of the mesh as expected due to the increased
317 distance of the targeted object.

318 Before exporting the DOM, the mesh was manually cleaned, in order to suppress rough
319 edges and "floating" polygons generated on the margins of the model. These artefacts on the
320 edges of the models were expected due to the photogrammetric "projection" process and the
321 remote point of view of the rover relative to these areas (e.g. Ullman, 1979; Westoby *et al.*,
322 2012). After this step, the overall area of the model decreased from ~2780 m² to a useful area
323 of 1625.8 m². The mesh was then exported in Wavefront .OBJ format to be used in other
324 softwares, along with its 8 textures as .JPG images, and an associated .MTL library file. While
325 the overall model presents a very high quality and accuracy in its textures, we do see some
326 texture stretching in the outermost parts of the DOM. These stretches were expected
327 particularly on the borders, on very complex shapes and in remote areas far from the rover due
328 to the distance and the reduced number of points of view (e.g. Valanis *et al.*, 2010). Moreover,
329 as our DOM was reconstructed using several sets of images with varying optical parameters,
330 an increased risk of such texturing artefacts was also expected. Indeed, some localized and
331 restricted areas whose relief was computed using one set (e.g. Navcam) could end up not being
332 textured correctly with another set (e.g. Mastcam), thus explaining some of the stretching
333 observed on the model (like the sandstone bed on the northwesternmost edge of the model, Fig.
334 4). However, after comparison with the source 2D material, this localized stretching does not
335 affect the geologically critical parts of the DOM, and therefore does not prevent their
336 characterization.

337 A textured low-resolution version of the Kimberley DOM can be seen on the Sketchfab
338 public repository using this link: https://skfb.ly/6KNq8.

339 When available, MAHLI microscopic images have to be processed separately as their
340 field of view is most often too small to be correlated with Mastcam and Navcam images.

341

342 4.5. Validation of scaling and georeferencing

343 Even though PhotoScan Professional is able to scale, level and position the 3D model
344 using the absolute spatial position of the georeferenced cameras, a verification is needed to
345 validate the correct localization and dimension of the model. On Earth, the use of markers of a
346 given size and/or Ground Control Points (GCP) with fixed and predetermined GPS-controlled
347 coordinates makes the scaling much more straightforward (e.g. Tavani *et al.*, 2016; James *et*
348 *al.*, 2018; Triantafyllou *et al.*, 2019). However, on Mars, no such tools are available, and we
349 therefore rely only on indirect observations and/or cross comparisons with orbital imagery (e.g.
350 HiRISE high-resolution orthoimages) to validate our scaling. This is for example achieved by
351 using *Curiosity*'s wheels tracks (wheels are 40 cm wide, Heverly *et al.*, 2013), which are
352 present on several images and therefore on the final texture (Fig. 4; see Appendix A3).

353 The scaling, leveling and positioning of the Kimberley DOM were therefore validated
354 using the CloudCompare software to align our DOM to the HiRISE DEM and within the Mars
355 2000 IAU system, which will be useful for direct integration into VR environments (see
356 below). This alignment against the HiRISE DEM allowed us to observe a nearly perfect
357 alignment between the photogrammetric DOM and the orbital DEM, with the only noticeable
358 exception being a sandstone bed on the northern flank of Mt. Remarkable (Fig. 4) situated on
359 the edge of the model, where distortion is expected due to the photogrammetric process and
360 rover's remote point of view. This distortion aside, the DOM show a remarkable consistency
361 and accuracy throughout the model, with a quantified relative scale offset as low as 1% between
362 the DOM and the DEM (see Tables S1 and S1 in Appendix A3).

363

364 Figure 4 (color online, 1.5 column):

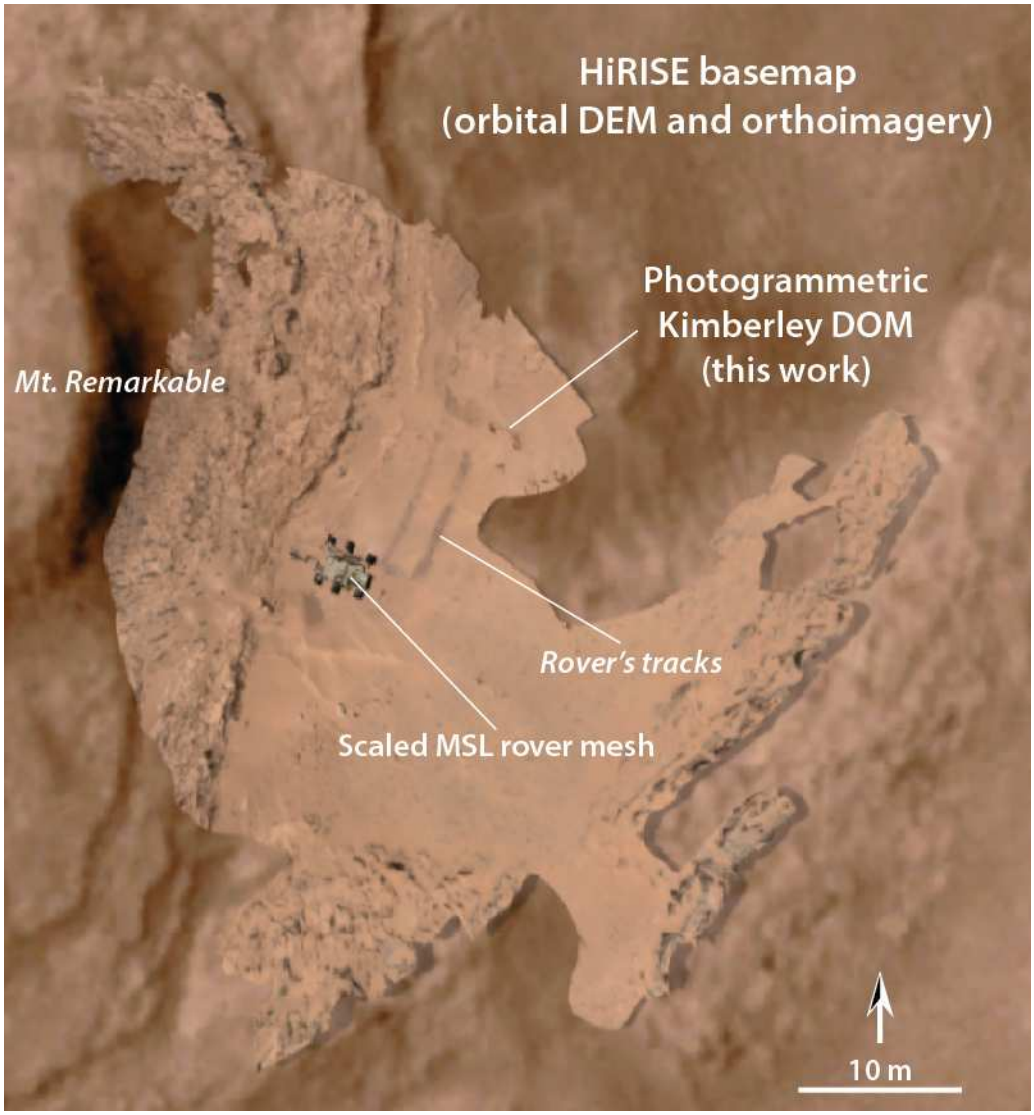

Figure 4: High-resolution full color DOM of the Kimberley outcrop, scaled and fitted on the georeferenced and scaled HiRISE DEM of the Gale crater, showing nearly perfect alignment between the two meshes (with exception for the northernmost part of Mt. Remarkable). A 1:1 mesh of the *Curiosity* rover is placed for scale.

5. Virtual reality exploration and characterization of the Kimberley DOM

5.1. Integration of the DOM into a VR environment

375 The use of Virtual Reality (VR) in planetary sciences is not a recent idea (McGreevy,
376 1993), but in the past three years, hardware and software developments as well as the
377 democratization of powerful computing units made it more accessible to our community.
378 Recently, several low-cost solutions were made available to enable a quick and easy VR
379 experience using publicly-available dedicated game-based engines (e.g. Mat *et al.*, 2014;
380 Murray, 2017), that provide an easy and fast solution to produce a VR scene.

381 In this work, the Kimberley DOM has been integrated into a VR scene simulating the
382 local environment of the real outcrop and its surroundings (Figs. 4 and 5). First, an extract
383 (~3x3 km square) of the HiRISE orbital DEM draped with the corresponding orthoimage is
384 integrated as a 3D basemap, making the middle-ground of the scene. This first layer represents
385 the local to regional context of the outcrop as well as giving ground-based landmarks for
386 orientation (e.g. Mt. Christine on Fig. 5a). The main component of the scene is composed by
387 the high-resolution DOM produced from ground images (Figs. 4, 5a and 5b). An additional
388 photogrammetric mesh of the Windjana drill hole, computed using a standalone set of 32
389 MAHLI microscopic images is also integrated to locally add a sub-mm-scale level of detail
390 (Fig. 5c). This model can be seen on the Sketchfab public repository using this link:
391 https://skfb.ly/6MqBy. In this localized inset in Figure 6c, we can even see the markings left
392 by the Laser Induced Breakdown spectroscopy (LIBS) measurements performed by the
393 ChemCam instrument (Maurice *et al.*, 2012) on the drill tailings and within the 1.6-cm in
394 diameter drill hole. All these models were integrated following geospatial alignment validation
395 using the CloudCompare software as described in §4.5.

396 Figure 6 shows several views of the resulting scene, as observed through a VR headset.
397 We added a 1:1 scale 3D mesh of *Curiosity* to help figuring out the real scale of the different
398 geological features. Moreover, this VR scene supports networked experience, enabling "multi-
399 users" collaborative work regardless of their physical emplacement, as illustrated on Figure 6b.

Figure 5 (color online, 1.5 column):

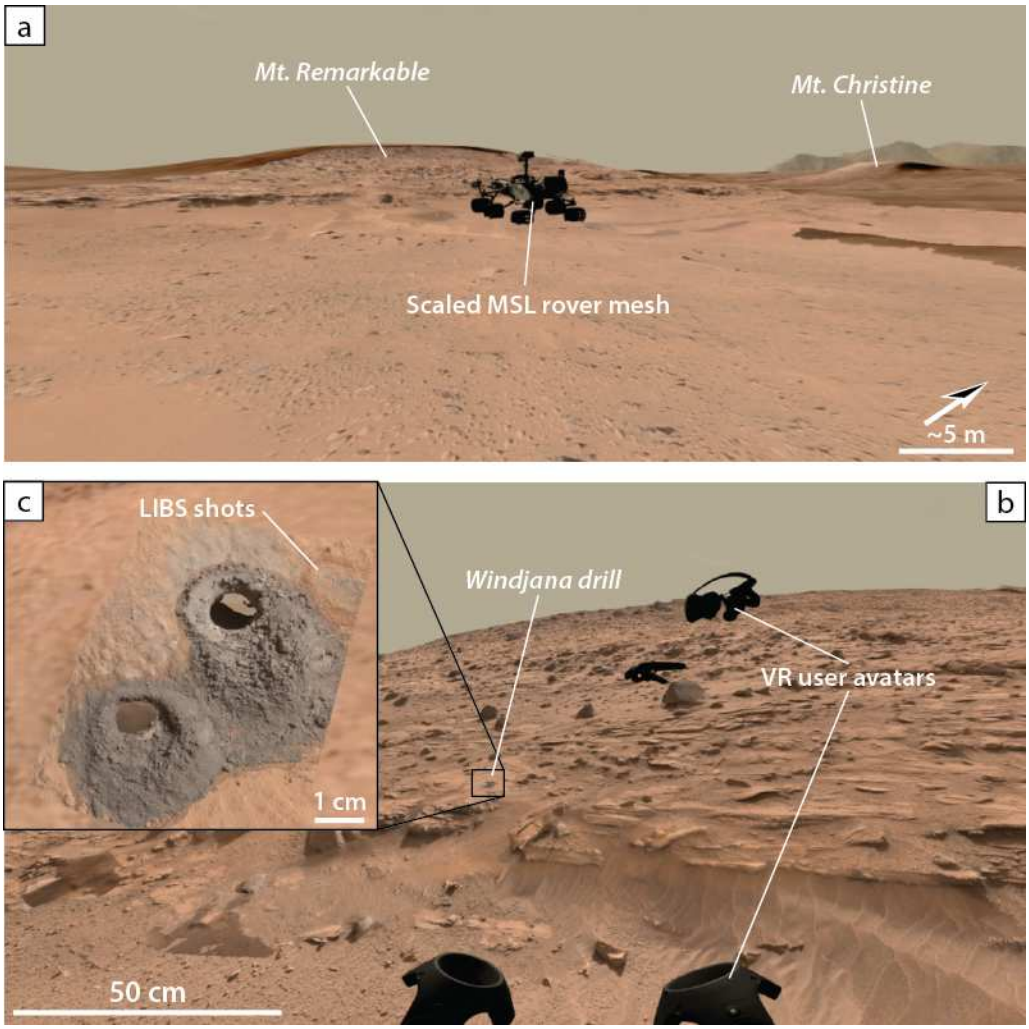

Figure 5: a) General view of the Kimberley simulated outcrop within the VR environment. Foreground high-resolution mesh is this work's DOM, middle-ground lower resolution model is the HiRISE DEM. The *Curiosity* rover mesh is placed for scale. b) Close-up view off the simulated outcrop toward the Windjana drill at the base of Mt. Remarkable. In this view, two users are exploring the outcrop in VR and their avatar representing hand controllers and headsets can be seen. c) Detailed view of the very high-resolution MAHLI mesh of the Windjana drill. The sub-mm-scale resolution allows to see the very small marks left by the Laser-Induced Breakdown Spectroscopy (LIBS) shots on the 3D mesh (<1 mm).

412

413 5.2. First insights toward a “field geology” characterization of the Kimberley outcrop in VR

414

415 One of the main assets of VR over classical viewing methods is the ability to observe
416 the real geometry of several geological structures (e.g. ripples, cross-stratifications, laterally
417 evolving trends in size or distribution). The latter are usually prevented using 2D panoramic
418 images that generate unavoidable deformations and limited point of view. While the use of a
419 3D non-static model brings valuable insights to the characterization of the 3D measure, shape
420 and structures of the reconstructed DOM, VR enables a real scale experience of the simulated
421 outcrops, which is useful in replacing geological features in their local to regional context, as
422 well as allowing varying ranges of projection and correlation and the ability to change the
423 viewer’s point of view. The use of VR therefore represents a significant advance for the *in-situ*
424 analysis of remote outcrops like Kimberley as geological field sites.

425

426 *5.2.1. VR section logging of the Mt. Remarkable*

427

428 Figure 6 shows a VR snapshot of the base of Mt. Remarkable featuring the Square Top,
429 Dillinger, Mt. Remarkable and Beagle members of the upper Kimberley series (Le Deit *et al.*,
430 2016; Stack *et al.*, 2016, Rice *et al.*, 2017). Precise characterization of the contacts between
431 each of these members is spatially restricted when using 2D images due to the limited points
432 of view and especially the presence of the regolith and dust covering most parts of the outcrop.
433 Within the VR environment, we were able to newly identify several stratified contacts that are
434 barely visible in the original images, allowing us to make a precise mapping of both the lower
435 and upper contacts of the Dillinger member around Mt. Remarkable (Fig. 6a). Indeed, the VR
436 allows users to walk around the outcrop without limitation and thus make possible visual

437 correlations over several meters to interpret the position of the contacts under the dust cover.
438 With this new mapping, we were also capable of making new and more accurate measurement
439 of the thickness of the Dillinger member using a dedicated measurement tool. Previous
440 approximation of this measure using images only was estimated to be “around half a meter”
441 (Fig. 6b; Le Deit *et al.*, 2016). Here, we end up with a new measure with a cm-scale precision,
442 which is 0.94 m thick (Fig. 6c).

443 VR also provides a mean for the contextualization of the various sampling performed
444 by *Curiosity*, such as the Windjana drill hole. Figure 6a shows the exact size and position of
445 this drill (within the lower part of the Dillinger member), so the user can see where the
446 geochemical experiments were performed, such as the ChemCam LIBS measurements (Fig.
447 5c). This information can be critical for further interpretations of the data for
448 paleoenvironmental reconstructions.

449

450 Figure 6 (color online, 2 columns):

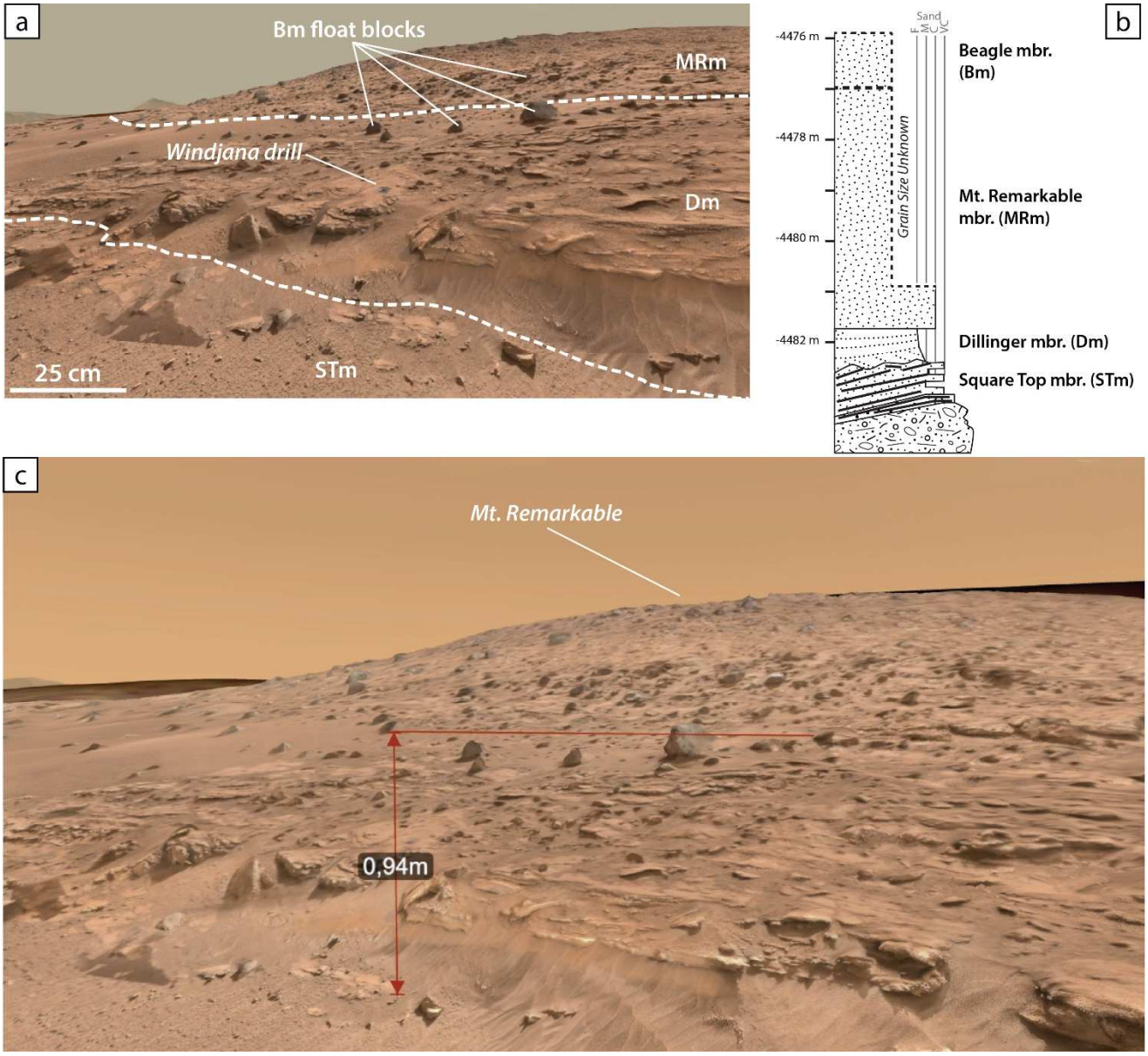

451

452

453 Figure 6: a) Interpreted VR panorama of the Mt. Remarkable showing the contacts between
454 Square Top, Dillinger and Mt. Remarkable members of the Kimberley formation (dashed white
455 line), and position of Beagle member float rocks. VR simulated outcrop enabled a precise
456 mapping of these contacts despite the presence of regolith and dust cover. b) Synthetic log of
457 the Kimberley formation at the Mt. Remarkable (after Le Deit *et al.*, 2016). c) VR view of the
458 Mt. Remarkable and measurement of the thickness of the Dillinger member using dedicated
459 tool within the VR environment.

460

461 *5.2.2. Characterization of multiscale sedimentary structures at Kimberley*

462

463 Using the VR environment, it is possible to freely and realistically navigate on and
464 around the real-scale 3D representation of the Kimberley outcrop, and to appreciate the distance
465 between the different parts of the outcrops. We can therefore make observations from multiple
466 points of view, as if we were on the field. This includes but is not limited to the identification
467 and characterization/measurement of the different geological features present at Kimberley, e.g.
468 stratigraphic (un-)conformable contacts, sedimentary structures of various scales (planar
469 laminations, cross-bedding, etc.) or even dm-scale gullies; but also assessing the 3D parameters
470 such as spatial repartition, orientation, dip and strike of these features. VR also enables spatial
471 projection of the outcrop within its immediate to local environment, allowing for a more
472 insightful understanding of the geometrical and stratigraphic relations within and around the
473 outcrop. The latter couldn't be readily approached by the use of conventional panoramic
474 imagery nor even using a non-static 3D DOM rendered on a 2D.

475 The figure 7, focuses on the metric-scale clinoforms present on the eastern part of the
476 outcrop and previously mentioned in the literature (Rice *et al.*, 2017). VR "line-drawing" of the
477 different sandstone beds allows us to characterize 6 different sets of dm-scale downlapping
478 cross-laminations (yellow lines on Fig. 7a), bounded by erosive angular unconformities (blue
479 lines on Fig. 7a). The 5 lower sets show a northwards prograding downlapping deposition over
480 bottom angular unconformities (bearing an angle of ~30°; Fig. 7b). Nearly all cross-laminations
481 across the 5 lower sets show a marked top truncation by a common unconformity (Fig. 7a),
482 delimitating a sixth upper set, with similar internal organization and presence of downlapping
483 cross-lamination. However, this set shows much lower angle of deposition and a reversed
484 southwards propagation direction. Those characteristics and internal organization, as well as
485 the fine to coarse sandstone lithology of the area (e.g. Le Deit *et al.*, 2016, Rice *et al.*, 2017)

are similar to that of aeolian dunes fields, with the bottom erosive unconformities possibly being reactivation surfaces (e.g. Ellwood *et al.*, 1975; Ewing & Korucek., 2010). This interpretation complements previous conclusions for this area (Grotzinger *et al.*, 2015; Rubin *et al.*, 2015).

Figure 7 (color online, 2 columns):

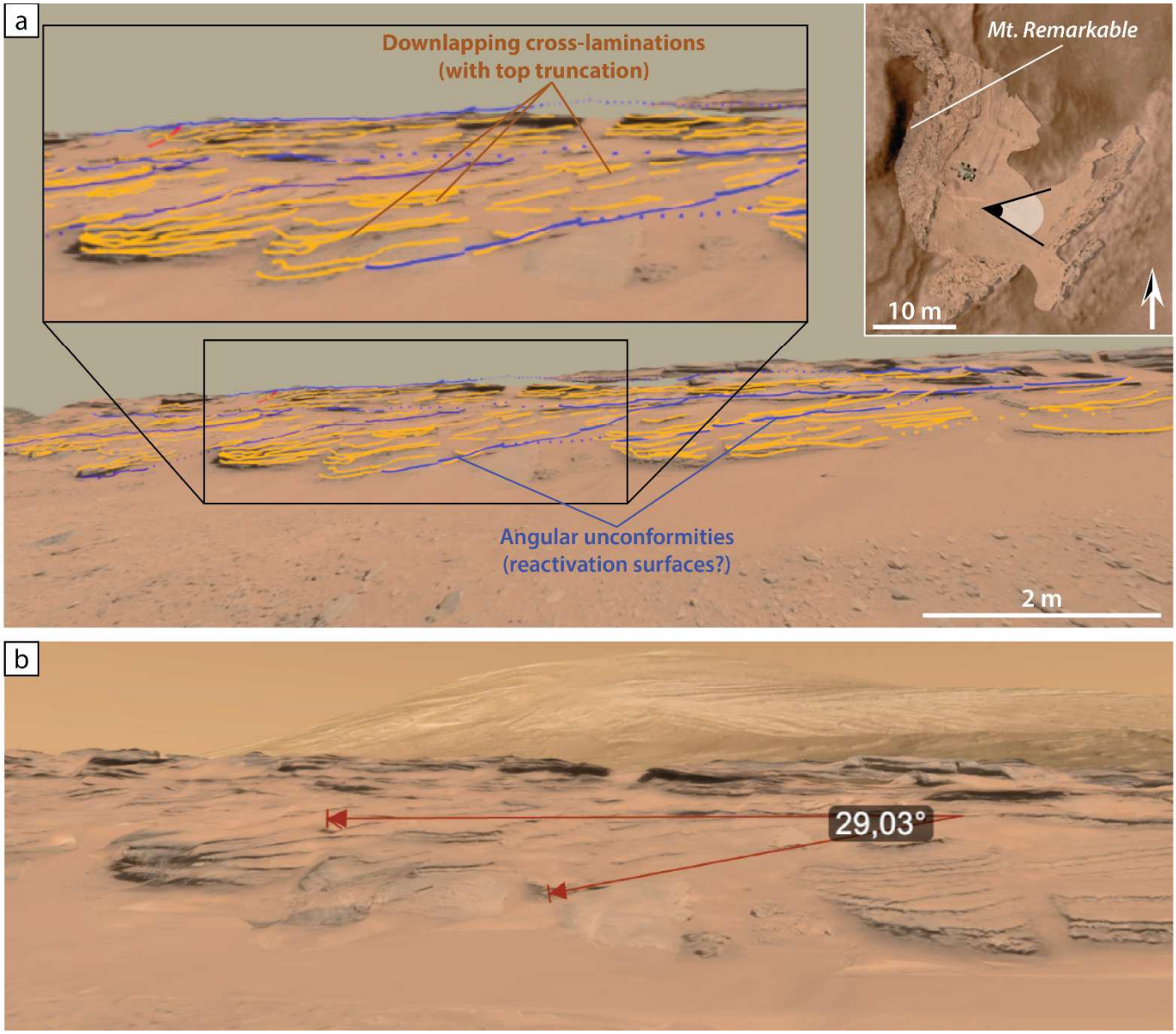

Figure 7: a) Interpreted VR panorama of the eastern part of the Kimberley outcrop (see embedded mini map for precise localization and point of view) with a VR "line-drawing" of the different sandstone beds observed. These beds are structured into 6 sets of downlapping

cross-stratifications, most being truncated at their top. These sets lie on a bottom erosive angular unconformity, interpreted as reactivation surfaces in a prograding system of dunes. The 5 lower sets prograde northwards, while the upper set, unconformably lying on top the others, progrades southwards. b) Detailed view of one set of cross-stratifications, and measurement of the dipping angle of its basal unconformity using dedicated tool within the VR environment.

Close observations on the Dillinger member allow to characterize cm-scale fine laminations within these finely-grained (fine to medium sands, Fig. 6b) dm-scale sandstone beds (Fig. 8). These cm-scale laminations have previously been characterized as forming "cross-stratifications" (Le Deit *et al.*, 2016; Stack *et al.*, 2016, Rice *et al.*, 2017). However, variations of the structures formed by the laminations can be seen, and cross-stratifications are not widespread across the beds. Figure 9 shows a S-N oriented catalog of cm-scale laminations observed within the Dillinger member at different locations on the outcrop. The southernmost part of the butte shows planar parallel laminations (Figs. 8a and 8b). Northwards, this organization evolves and co-occurrent parallel and cross-stratified laminations are visible (Fig. 8c). Cross-stratifications are more conspicuous toward the northern part of the butte, with the presence of dm-scale structures organized as trough cross-stratification (TCS, Fig. 8d). These different structures within the Dillinger member therefore highlight lateral variations of the facies, that are compatible with an active fluvio-deltaic paleoenvironment as described in previous works (e.g. Grotzinger *et al.*, 2015; Rice *et al.*, 2017).

Lastly, no major unconformity was observed within this outcrop although observed under various angles. Only local truncations in relation with cross-bedding are observed along a generally continuous set of sedimentary deposits. While not definitive given the local aspect of the DOM used, these observations are not consistent with the assumption made in Williams

et al. (2018) that the upper section of the outcrop could belong to younger deposits. Further work with larger DOM will enable to confirm and detail some of these observations.

Figure 8 (color online, 2 columns):

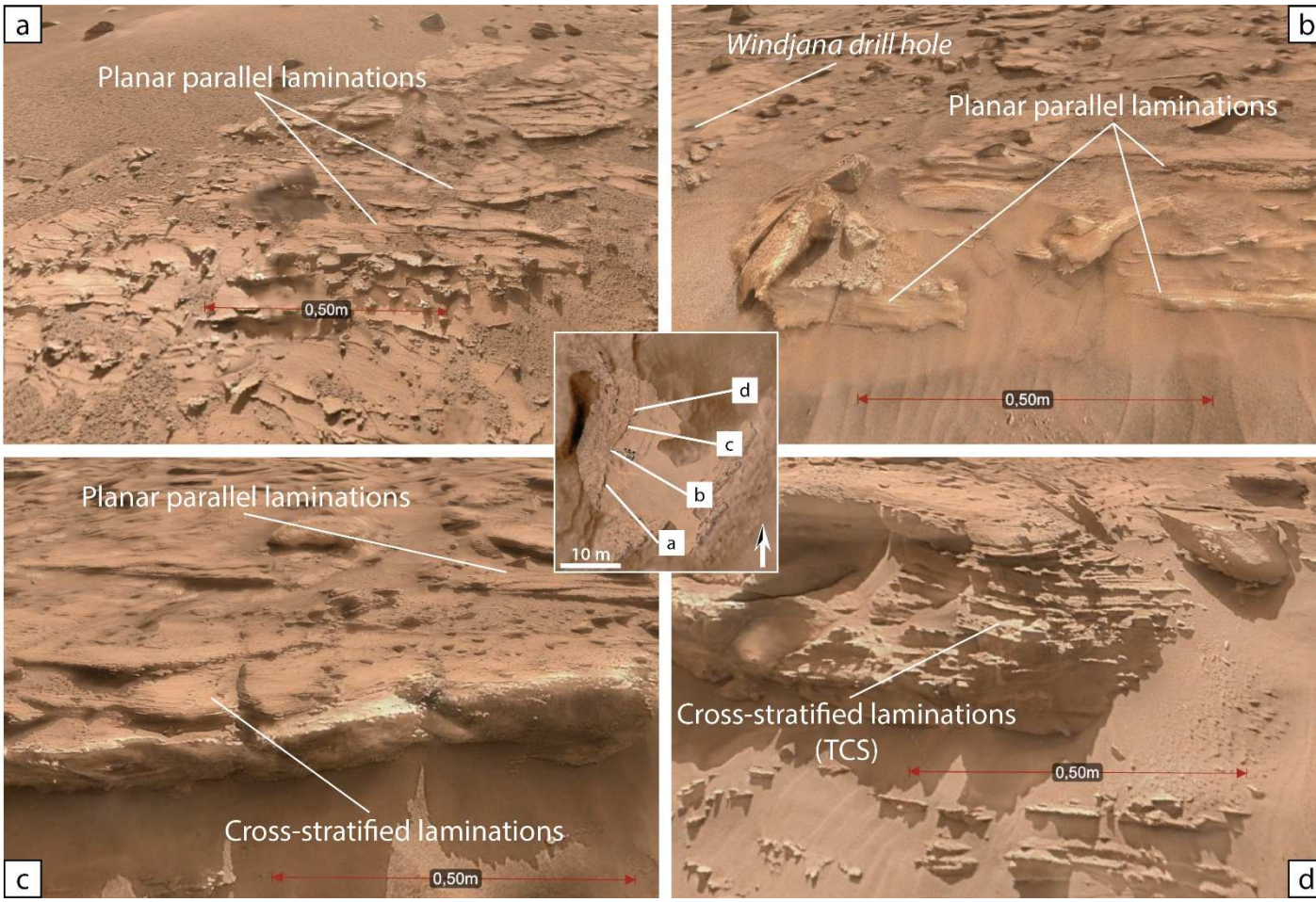

Figure 8: Detailed views of the Dillinger member at the base of Mt. Remarkable showing the evolution of sedimentary structures within the sandstone beds, highlighting lateral variations of the facies. Scale bar is given using dedicated tool within the VR environment. a) Southernmost part of the Dillinger member, showing planar parallel laminations. b) Planar parallel lamination near the Windjana drill hole. c) Co-occurrence of planar parallel and cross-stratified laminations toward the northern part of the Dillinger member. d) Trough Cross-Stratifications (TCS) in the northernmost part of the simulated outcrop.

6. Conclusion and perspectives

In this work, we described the reconstruction of a multi-scale, highly resolved Digital Outcrop Model of the Kimberley outcrop using a dataset comprising 2005 images taken by four different cameras aboard Mars Science Laboratory rover *Curiosity*. Despite their differences in optical parameters, a step-by-step iterative workflow using Agisoft PhotoScan SfM photogrammetry software proved successful to obtain a scaled full color highly-resolved DOM of the outcrop. A low resolution version of this DOM is available on the Sketchfab website (https://skfb.ly/6KNq8), as well as the Windjana drill micro-model (https://skfb.ly/6MqBy).

The DOM was thereafter integrated within a Virtual Reality environment allowing the immersion and real scale visualization of the simulated outcrop, for both research and educational purposes. One or several users can walk and investigate the outcrop as if they were "in the field", to enable geological observations and interpretations based on the realistic depiction of the actual geometries.

The overall quality of the model coupled with new dedicated VR measurement tools allow us to observe and characterize several significant previously underrated geomorphological and sedimentological features such as structured laminations and (un-) conformable contacts. This represents a first step toward a better understanding of the intra- and inter-formational relations of the Kimberley series. The next step is the continuing development of innovative quantitative measurement tools directly useable in VR (compass, telemeter, clinometer, etc.), so as multi-layer functionalities such as in Geographical Information Systems and compatibility with the latter. These VR techniques are paving the way for remote geological exploration and characterization of Martian or other planetary outcrops in near future.

Acknowledgements

We acknowledge two anonymous reviewers for their constructive suggestions that helped improve the manuscript. This work was supported by the European Commission Research Executive Agency under the Horizon 2020 “PlanMap” project (grant n° 776276). We also acknowledge the support from the French Spatial Agency (CNES). Data used in this study are publicly available on the Planetary Data System (https://pds.nasa.gov/).

References

Agisoft, LLC, 2018. PhotoScan Professional. https://www.agisoft.com, Accessed: 10 October 2018.

Alexander, D. & Deen, R., 2015. Mars Science Laboratory Project Software Interface Specification (SIS); Camera & LIBS Experiment Data Record (EDR) and Reduced Data Record (RDR) Data Products, version 3.0. *NASA Planetary Data System*. URL: https://pds-imaging.jpl.nasa.gov/data/msl/MSLNAV_0XXX/DOCUMENT/MSL_CAMERA_SIS_latest.PDF

Arbués, P., García-Sellés, D., Granado, P., López-Blanco, M., Muñoz, J., 2012. A method for producing photorealistic digital outcrop models. In *74th EAGE Conference and Exhibition incorporating EUROPEC 2012*, Abstract #D029. DOI: 10.3997/2214-4609.20148218

Banham, S. G., Gupta, S., Rubin, D. M., Watkins, J. A., Sumner, D. Y., Edgett, K. S., Grotzinger, J. P., Lewis, K. W., Edgar, L. A., StackMorgan, K. M., Barnes, R., Bell, J. F., Day, M. D., Ewing, R. C., Lapotre, M., Stein, N. T., Rivera-Hernandez, F., Vasavada, A. R., 2018. Ancient Martian aeolian processes and palaeomorphology reconstructed from the Stimson formation on the lower slope of Aeolis Mons, Gale crater, Mars. *Sedimentology* **65**(4), 993-1042. DOI: 10.1111/sed.12469

Bell III, J. F., Godber, A., Rice, M. S., Fraeman, A. A., Ehlmann, B. L., Goetz, W., Hardgrove, C. J., Harker, D. E., Johnson, J. R., Kinch, K. M., Lemmon, M. T., McNair, S., Le Mouélic, S., Madsen, M. B., Malin, M. C., MSL Science Team, 2013. Initial multispectral imaging results from the Mars Science Laboratory Mastcam investigation at the Gale crater field site. In *Lunar and Planetary Sciences*

Conference 44, Abstract #1719, 1417. URL: https://www.lpi.usra.edu/meetings/lpsc2013/pdf/1417.pdf

Bemis, S. P., Micklethwaite, S., Turner, D., James, M. R., Akciz, S., Thiele, S. T., Bangash, H. A., 2014. Ground-based and UAV-based photogrammetry: A multi-scale, high-resolution mapping tool for structural geology and paleoseismology. *Journal of Structural Geology*, **69**, 163-178. DOI: 10.1016/j.jsg.2014.10.007

Billant, J., Leclerc, F., Escartin, J., Gracias, N., Istenic, K., Garcia, R., Arnaubec, A., Dano, A., Marchand, C., SUBSAINTES science party, 2019. Development of a Unity package allowing GIS-like mapping in Virtual Reality environment. In *Geophysical Research Abstract* **21**, Abstract #EGU2019-13639-3. URL: https://meetingorganizer.copernicus.org/EGU2019/EGU2019-13639-3.pdf

Bristow, T.F., Rampe, E.F., Achilles, C.N., Blake, D.F., Chipera, S.J., Craig, P., Crisp, J.A., Des marais, D.J., Downs, R.T., Gellert, R., Grotzinger, J.P., Gupta, S., Hazean, R.M., Horgan, B., Hogancamp, J.V., Mangold, N., Mahaffy, P.R., McAdam, A.C., Ming, D.W., Morookian, J.M., Morris, R.V., Morrison, S.M., Treiman, A.H., Vaniman, D.T., Vasavada, A.R., Yen, A.S., 2018. Clay mineral diversity and abundance in sedimentary rocks of Gale Crater, Mars. *Science Advances* **4**(6), eaar:3330. DOI: 10.1126/sciadv.aar3330

Calef III, F.J., Parker, T., 2016, MSL Gale Merged Orthophoto Mosaic, Publisher: PDS Annex, U.S. Geological Survey, URL: http://bit.ly/MSL_Basemap

Carr, B. B., Clarke, A. B., Arrowsmith, J. R., Vanderkluysen, L., Dhanu, B. E., 2019. The emplacement of the active lava flow at Sinabung Volcano, Sumatra, Indonesia, documented by structure-from-motion photogrammetry. *Journal of Volcanology and Geothermal Research*, **382**, 164-172. DOI: 10.1016/j.jvolgeores.2018.02.004

Carrivick, J. L., Smith, M. W., Quincey, D. J., 2016. *Structure from Motion in the Geosciences*. John Wiley & Sons.

Edgett, K. S., Caplinger, M. A., Maki, J. N., Ravine, M. A., Ghaemi, F. T., McNair, S., Herkenhoff, K. E., Duston, B. M., Willson, R. G., Yingst, R. A., Kennedy, M. R., Minitti, M. E., Sengstacken, A. J., Supulver, K. D., Lipkaman, L. J., Krezoski, G. M., McBride, M. J., Jones, T. L., Nixon, B. E., Van Beek, J. K., Krysak, D. J., Kirk, R. L., 2015. Curiosity's robotic arm-mounted Mars Hand Lens Imager (MAHLI): Characterization and calibration status. MSL MAHLI Technical Report 0001 (19 June 2015). DOI: 10.13140/RG.2.1.3798.5447

621 Ellwood, J. M., Evans, P. D., Wilson, I. G., 1975. Small scale aeolian bedforms. *Journal of*
622 *Sedimentary Research* **45**(2), 554-61. DOI: 10.1306/212F6DCA-2B24-11D7-
623 8648000102C1865D
624 Ewing, R. & Kocurek, G., 2010. Aeolian dune-field pattern boundary conditions.
625 *Geomorphology* **114**(3), 175-87. DOI : 10.1016/j.geomorph.2009.06.015
626 Favalli, M., Fornaciai, A., Isola, I., Tarquini, S., Nannipieri, L., 2012. Multiview 3D
627 reconstruction in geosciences. *Computers & Geosciences* 44, 168-76. DOI:
628 10.1016/j.cageo.2011.09.012
629 Fraeman, A.A., Ehlmann, B.L., Arvidson, R.E., Edwards, C.S., Grotzinger, J.P., Milliken,
630 R.E., Quinn, D.P., Rice, M.S., 2016. The stratigraphy and evolution of lower Mount
631 Sharp from spectral, morphological, and thermophysical orbital data sets. *Journal of*
632 *Geophysical Research: Planets* **121**, 1713-1736. DOI: 10.1002/2016JE005095
633 Gerloni, I.G., Carchiolo, V., Vitello, F.R., Sciacca, E., Becciani, U., Costa, A., Riggi, S.,
634 Bonali, F.L., Russo, E., Fallati, L., Marchese, F., Tibaldi, A., 2018. Immersive
635 Virtual Reality for Earth Sciences. In *2018 Federated Conference on Computer*
636 *Science and Information Systems (FedCSIS)* **15**, 527-534. DOI: 10.15439/2018F139
637 Girardeau-Montaut, D., 2015. Cloud compare—3d point cloud and mesh processing software.
638 *Open Source Project*. EDF R&D, Telecom ParisTech. URL:
639 http://www.danielgm.net/cc
640 Grotzinger, J. P. , Sumner, D. Y., Kah, L. C., Stack, K., Gupta, S., Edgar, L., Rubin, D.,
641 Lewis, K., Schieber, J, Mangold, N., Milliken, R., Conrad, P. G., DesMarais, D.,
642 Farmer, J., Siebach, K., Calef III, F., Hurowitz, J., McLennan, S. M., Ming, D.,
643 Vaniman, D., Crisp, J., Vasavada, A., Edgett, K. S., Malin, M., Blake, D., Gellert, R.,
644 Mahaffy, P., Wiens, R. C., Maurice, S., Grant, J. A., Wilson, S., Anderson, R. C.,
645 Beegle, L., Arvidson, R., Hallet, B., Sletten, R. S., Rice, M., Bell III, J. F., Griffes, J.,
646 Ehlmann, B., Anderson, R. B., Bristow, T. F., Dietrich, W.E., Dromart, G.,
647 Eigenbrode, J., Fraeman, A., Hardgrove, C., Herkenhoff, K., Jandura, L., Kocurek,
648 G., Lee, S., Leshin, L. A., Leveille, R., Limonadi, D., Maki, J., McCloskey, S.,
649 Meyer, M., Minitti, M., Newsom, H., Oehler, D., Okon, A., Palucis, M., Parker, T.,
650 Rowland, S., Schmidt, M., Squyres, S., Steele,A., Stolper, E., Summons, R.,
651 Treiman, A., Williams, R., Yingst, A., MSL Science Team, 2014. A Habitable
652 Fluvio-Lacustrine Environment at Yellowknife Bay, Gale Crater, Mars. *Science*
653 **343**(6169), 1242777. DOI: 10.1126/science.1242777

Grotzinger, J., Gupta, S., Malin, M., Rubin, D., Schieber, J., Siebach, K., Sumner, D., Stack, K., Vasavada, A., Arvidson, R., Calef III, F., Edgar, L., Fisher, W. F., Grant, J. A., Griffes, J., Kah, L. C., Lamb, M. P., Lewis, K. W., Mangold, N., Minitti, M. E., Palucis, M., Rice, M., Williams, R. M. E., Yingst, R. A., Blake, D., Blaney, D., Conrad, P., Crisp, J., Dietrich, W. E., Dromart, G., Edgett, K. S., Ewing, R. C., Gellert, R., Hurowitz, J. A., Korucek, G., Mahaffy, P., McBride, M. J., McLennan, S. M., Mischna, M., Ming, D., Milliken, R., Hewsom, H., Orhler, D., Parker, T. J., Vaniman, D., Wiens, R. C., Wilson, S.A., 2015. Deposition, exhumation, and paleoclimate of an ancient lake deposit, Gale crater, Mars. *Science* **350**(6257), aac7575. DOI: 10.1126/science.aac7575

Harvey, P., 2013. ExifTool: Read, write and edit meta information. https://www.sno.phy.queensu.ca/~phil/exiftool/

Heverly, M., Matthews, J., Lin, J., Fuller, D., Maimone, M., Biesiadecki, J., Leichty, J., 2013. Traverse performance characterization for the Mars Science Laboratory rover. *Journal of Field Robotics* **30**(6), 835-46. DOI: 10.1002/rob.21481

James, M. R., Robson, S., d'Oleire-Oltmanns, S., Niethammer, U., 2017. Optimising UAV topographic surveys processed with structure-from-motion: Ground control quality, quantity and bundle adjustment. *Geomorphology*, **280**, 51-66. DOI: 10.1016/j.geomorph.2016.11.021

Le Deit, L., Mangold, N., Forni, O., Cousin, A., Lasue, J., Schröder, S., Wiens, R. C., Sumner, D., Fabre, C., Stack, K. M., Anderson, R. B., Blaney, D., Clegg, S., Dromart, G., Fisk, M., Gasnault, O., Grotzinger, J. P., Gupta, S., Lanza, N., Le Mouélic, S., Maurice, S., McLennan, S., Meslin, P.-Y., Nachon, M., Newsom, H., Payré6, V., Rapin, W., Rice, M., Sautter, V., Treiman17, A. H., 2016. The potassic sedimentary rocks in Gale Crater, Mars, as seen by ChemCam on board *Curiosity*. *Journal of Geophysical Research: Planets* **121**. DOI: 10.1002/2015JE004987

Le Mouélic, S., Gasnault, O., Herkenhoff, K. E., Bridges, N. T., Langevin, Y., Mangold, N., Maurice, S., Wiens, R. C., Pinet, P., Newsom, H. E., Deen, R. G., Bell III, J. F., Johnson, J. R., Rapin, W., Barraclough, B., Blaney, D. L., Deflores, L., Maki, J., Malin, M. C., Pérez, R., Saccoccio, M., 2015. The ChemCam Remote Micro-Imager at Gale Crater: Review of the first year of operation on Mars. *Icarus* **249**, 93-107. DOI: 10.1016/j.icarus.2014.05.030

686 Maki, J., Thiessen, D., Pourangi, A., Kobzeff, P., Litwin, T., Scherr, L., Elliott, S., Dingizian,
687 A., Mainome, M., 2012. The Mars Science Laboratory Engineering Cameras. *Space*
688 *Science Reviews* **170**(1-4), 77-93. DOI: 10.1007/s11214-012-9882-4
689 Malin, M. C., Caplinger, M. A., Edgett, K. S., Ghaemi, F. T., Ravine, M. A., Schaffner, J. A.,
690 Baker, J. M., Bardis, J. D., Dibiase, D. R., Maki, J. N., Willson, R. G., Bell III, J. F.,
691 Dietrich, W. E., Edwards, L. J., Hallet, B., Herkenhoff, K. E., Heydari, E., Kah, L.
692 C., Lemmon, M. T., Minitti, M. E., Olson, T. S., Parker, T. J., Rowland, S. K.,
693 Schieber, J., Sullivan, R. J., Sumner, D. Y., Thomas, P. C., Yingst, R. A., 2010. The
694 Mars Science Laboratory (MSL) Mast-mounted Cameras (Mastcams) Flight
695 Instruments. Lunar and Planetary Sciences Conference 41, Abstract #1533, 1123.
696 URL: https://www.lpi.usra.edu/meetings/lpsc2010/pdf/1123.pdf
697 Mangold, N., Forni, O., Dromart, G., Stack, K., Wiens, R. C., Gasnault, O., Sumner, D. Y.,
698 Nachon, M., Meslin, P. Y., Anderson, R. B., Barraclough, B., Bell III, J. F., Berger,
699 G., Blaney, D. L., Bridges, J. C., Calef III, F., Clark, B., Clegg, S. M., Cousin, A.,
700 Edgar, L., Edgett, K., Ehlmann, B., Fabre, C., Fisk, M., Grotzinger, J., Gupta, S.,
701 Herkenhoff, K. E., Hurowitz, J., Johnson, J. R., Kah, L. C., Lanza, N., Lasue, J., Le
702 Mouélic, S., Léveillé, R., Lewin, E., Malin, M., McLennan, S., Maurice, S.,
703 Melikechi, N., Mezzacappa, A., Milliken, R., Hewsom, H., Ollila, A., Rowland, S.
704 K., Sautter, V., Schmidt, M., Chröder, S., d'Uston C., Vaniman, D., Williams, R.,
705 2015. Chemical variations in Yellowknife Bay formation sedimentary rocks analyzed
706 by ChemCam on board the Curiosity rover on Mars. *Journal of Geophysical*
707 *Research: Planets* **120**(3), 452-82. DOI: 10.1002/2014JE004681
708 Mangold, N., Schmidt, M.E., Fisk, M.R., Forni, O., McLennan, S.M., Ming, D.W., Sautter,
709 V., Sumner, D., Williams, A.J., Clegg, S.M., Cousin, A., Gasnault, O., Gellert, R.,
710 Grotzinger, J.P., Wiens, R.C., 2017. Classification scheme for sedimentary and
711 igneous rocks in Gale Crater, Mars. *Icarus* **284**, 1-17. DOI:
712 10.1016/j.icarus.2016.11.005
713 Martell, A., Lauterbach, H. A., Schilling, K., Nuchtcer, A., 2018. Benchmarking structure
714 from motion algorithms of urban environments with applications to reconnaissance
715 in search and rescue scenarios. In *2018 IEEE International Symposium on Safety,*
716 *Security, and Rescue Robotics (SSRR)* 1-7. DOI: 10.1109/SSRR.2018.8468612
717 Mat, R. C., Shariff, A. R. M., Zulkifli, A. N., Rahim, M. S. M., Mahayudin, M. H., 2014.
718 Using game engine for 3D terrain visualization of GIS data: A review. In *IOP*

Conference Series: Earth and Environmental Science **20**, 012037. URL: https://iopscience.iop.org/article/10.1088/1755-1315/20/1/012037/pdf

Maurice, S., Wiens, R.C., Saccoccio, M., Barraclough, B., Gasnault, O., Forni, O., Mangold, N., Baratoux, D., Bender, S., Berger, G., Bernardin, J., Berthé, M., Bridges, N., Blaney, D., Bouyé, M., Caïs, P., Clark, B., Clegg, S., Cousin, A., Cremers, D., Cros, A., DeFlores, L., Derycke, C., Dingler, B., Dromart, G., Dubois, B., Dupieux, M., Durand, E., d'Uston, L., Fabre, C., Faure, B., Gaboriaud, A., Gharsa, T., Herkenhoff, K., Kan, E., Kirkland, L., Kouach, D., Lacour, J.-L., Langevin, Y., Lasue, J., Le Mouélic, S., Lescure, M, Lewin, E., Limonadi, D., Manhès, G., Mauchien, P., McKay, C., Meslin, P.-Y., Michel, Y., Miller, E., Newsom, H.E., Orttner, G., Paillet, A., Parès, L., Parot, Y., Pérez, R., Pinet, P., Poitrasson, F., Quertier, B., Sallé, B., Sotin, C., Sautter, V., Séran, H., Simmonds, J.J., Sirven, J.-B., Stiglich, R., Strieberg, N., Thocaven, J.-J., Toplis, M.J., Vaniman, D., 2012. The ChemCam instrument suite on the Mars Science Laboratory (MSL) rover: Science objectives and mast unit description. *Space Sci. Rev.*, **170**, 95-166, DOI 10.1007/s11214-012-9912-2.

McGreevy, M. W., 1993. Virtual reality and planetary exploration. In *Virtual Reality* pp. 163-97. Elsevier. DOI: 10.1016/B978-0-12-745045-2.50018-0

Micheletti, N., Chandler, J.H., Lane, S.N., 2015. Structure from motion (SFM) photogrammetry. *in*: Clarke, L.E. and Nield, J.M. (Eds.) Geomorphological Techniques (Online Edition). London: British Society for Geomorphology. ISSN: 2047-0371, Chap. 2, Sec. 2.2. URL: https://repository.lboro.ac.uk/articles/Structure_from_motion_SFM_photogrammetry/9457355

Murray, J. W., 2017. *Building virtual reality with Unity and Steam VR*. AK Peters/CRC Press. DOI: 10.1201/b21862

Ostwald, A. & Hurtado, J., 2017. 3D Models from Structure-from-Motion Photogrammetry Using Mars Science Laboratory Images: Methods and Implications. In *Lunar and Planetary Science Conference 48*, Abstract#1964, 1787. DOI: https://www.hou.usra.edu/meetings/lpsc2017/pdf/1787.pdf

Parker, T., Calef III, F.J., 2016, MSL Gale Merged Digital Elevation Model, Publisher: PDS Annex, U.S. Geological Survey, URL: http://bit.ly/MSL_DEM

Rice, M. S., Gupta, S., Treiman, A. H., Stack, K. M., Calef, F., Edgar, L. A., Grotzinger, J., Lanza, N., Le Deit, L., Lasue, J., Siebach, K. L., Vasavada, A., Wiens, R. C.,

752 Williams, J., 2017. Geologic overview of the Mars Science Laboratory rover mission
753 at the Kimberley, Gale crater, Mars. *Journal of Geophysical Research: Planets*
754 **122**(1), 2-20. DOI: 10.1002/2016JE005200
755 Rubin, D. M.; Grotzinger, J. P.; Gupta, S.; Sumner, D. Y.; Williams, R. M. E.; Dietrich, W.
756 E.; Edgar, L. A.; Lewis, K. W.; Oehler, D. Z.; Rice, M. S.; Schieber, J.; Stack, K.,
757 2015. Sedimentary facies as indicators of changing lake levels in Gale crater, Mars.
758 In *AGU Fall Meeting 2015*, Abstract P43B-2116.
759 Seidelmann PK, Abalakin VK, Bursa M, Davies ME, de Bergh C, Lieske JH, Oberst J, Simon
760 JL, Standish EM, Stooke P, Thomas P, 2002. Report of the IAU/IAG working group
761 on cartographic coordinates and rotational elements of the planets and satellites:
762 2000. *Celest Mech Dyn Astron* **82**(1):83–111. DOI: 10.1023/A:1013939327465
763 Stack, K. M., Edwards, C. S., Grotzinger, J. P., Gupta, S., Summer, D. Y., Calef III, F. J.,
764 Edgar, L. A., Edgett, K. S., Framan, A. A., Jacob, S. R., Le Deit, L., Lewis, K. W.,
765 Rice, M. S., Rubin, D., Williams, R. M. E., Williford, K. H., 2016. Comparing
766 orbiter and rover image-based mapping of an ancient sedimentary environment,
767 Aeolis Palus, Gale Crater, Mars. *Icarus* **280**, 3-21. DOI:
768 10.1016/j.icarus.2016.02.024.
769 Stein, N., Grotzinger, J., Schieber, J., Mangold, N., Hallet, B., Newsom, H., Stack, K., Berger,
770 J., Thompson, L., Siebach, K., Cousin, A., Le Mouélic, S., Minitti, M., Summer, D.
771 Y., Fedo, C., House, C. H., Gupta, S., Vasavada, A. R., Gellert, R., Wiens, R. C.,
772 Frydenvang, J., Forni, O., Meslin, P. Y., Payré, V., Dehouck, E., 2018. Desiccation
773 cracks provide evidence of lake drying on Mars, Sutton Island member, Murray
774 formation, Gale Crater. *Geology* **46**(6), 515-18. DOI: 10.1130/G40005.1
775 Szeliski, R., 2010. *Computer vision: algorithms and applications*. Springer Science &
776 Business Media. DOI: 10.1007/978-1-84882-935-0
777 Tavani, S., Corradetti, A., Billi, A., 2016. High precision analysis of an embryonic
778 extensional fault-related fold using 3D orthorectified virtual outcrops: The viewpoint
779 importance in structural geology. *Journal of Structural Geology* **86**, 200-210. DOI:
780 10.1016/j.jsg.2016.03.009
781 Tavani, S., Granado, P., Corradetti, A., Girundo, M., Iannace, A., Arbués, P., Muñoz, J. A.,
782 Mazzoli, S., 2014. Building a virtual outcrop, extracting geological information from
783 it, and sharing the results in Google Earth via OpenPlot and Photoscan: An example

from the Khaviz Anticline (Iran). *Computers & Geosciences* **63**, 44-53. DOI: 10.1016/j.cageo.2013.10.013

Treiman, A. H., Bish, D.L., Taniman, D.T., Chipera, S.J., Blake, D.F., Ming, D.W., Morris, R.V., Bristow, R.W., Morrison, S.M., Baker, M.B., Rampe, E.B., Downs, R.T., Filiberto, J., Glazner, A.F., Gellert, R., Thompson, L.M., Schmidt, M.E., Le Deit, L., Wiens, R.C., McAdam, A.C., Achilles, C.N., Edgett, K.S., Farmer, J.D., Fendrich, K.V., Grotzinger, J.P., Gupta, S., Morookian, J.M., Newcombe, M.E., Rice, M.S., Spray, J.G., Stolper, E.M., Sumner, D.Y., Vasavada, A.R., Yen, A.S., 2016. Mineralogy, provenance, and diagenesis of a potassic basaltic sandstone on Mars: CheMin X-ray diffraction of the Windjana sample (Kimberley area, Gale crater), *Journal of Geophysical Research: Planets* **121**, 75–106. DOI: 10.1002/2015JE004932.

Triantafyllou, A., Watlet, A., Le Mouélic, S., Camelbeeck, T., Civet, F., Kaufmann, O., Quinif, Y., Vandycke, S., 2019. 3-D digital outcrop model for analysis of brittle deformation and lithological mapping (Lorette cave, Belgium). *Journal of Structural Geology* **120**, 55-66. DOI: 10.1016/j.jsg.2019.01.001

Ullman, S., 1979. The interpretation of structure from motion. *Proceedings of the Royal Society of London. Series B. Biological Sciences* **203**(1153), 405-26. DOI: 10.1098/rspb.1979.0006

Valanis, A., Fournaros, S., Georgopoulos, A., 2010. Photogrammetric texture mapping of complex objects. *Proceedings of EuroMed2010 3rd International Conference dedicated on Digital Heritage*. URL: http://citeseerx.ist.psu.edu/viewdoc/download?doi=10.1.1.724.5752&rep=rep1&type=pdf

Verhoeven, G., 2011. Taking computer vision aloft–archaeological three-dimensional reconstructions from aerial photographs with photoscan. *Archaeological prospection* **18**(1), 67-73. DOI: 10.1002/arp.399

Vrublová, D., Kapica, R., Jiránková, E., Struś, A.,2015. Documentation of landslides and inaccessible parts of a mine using an unmanned UAV system and methods of digital terrestrial photogrammetry. *GeoScience Engineering*, **61**(3), 8-19. DOI: 10.1515/gse-2015-0018

Westoby, M. J., Brasington, J., Glasser, N. F., Hambrey, M. J., Reynolds, J., 2012. 'Structure-from-Motion'photogrammetry: A low-cost, effective tool for geoscience applications. *Geomorphology* **179**, 300-314. DOI: 10.1016/j.geomorph.2012.08.021

Williams, M.E., Malin, M.C., Stack, K.M., Rubin, D.M., 2018. Assessment of Aeolis Palus stratigraphic relationships based on bench-forming strata in the Kylie and the Kimberley regions of Gale Crater, Mars. *Icarus* **309**, 81-104. DOI: 10.1016/j.icarus.2018.02.028